EES Catalysis

PAPER

View Article Online
View Journal

Cite this: DOI: 10.1039/d5ey00269a

Understanding CO_2 reduction selectivity in silver and gold electrocatalysts using atomically precise nanoclusters

Hoeun Seong, †[a] Fang Sun,†[b] Qing Tang *[b] and Dongil Lee *[a]

Au and Ag electrodes have been widely utilized as catalysts for the electrochemical CO_2 reduction reaction (CO_2RR) in aqueous solutions. Despite significant differences in their CO_2RR and competing hydrogen evolution reaction (HER) activities, the fundamental reasons for these distinctions remain unclear. Herein, we present a comparative analysis employing atomically precise Ag and Au nanocluster (NC) catalysts, $Ag_{25}(SR)_{18}$ and $Au_{25}(SR)_{18}$ (where SR represents a thiolate ligand), to elucidate the molecular-level mechanisms governing the CO_2RR and the HER on Ag and Au surfaces. While $Au_{25}(SR)_{18}$ NCs demonstrate a lower onset potential for the CO_2RR compared to $Ag_{25}(SR)_{18}$ NCs, the CO current density of the $Au_{25}(SR)_{18}$ NCs reaches a plateau and even decreases at high overpotentials due to the increased HER. Electrokinetic and *in situ* infrared spectroscopy investigations using well-defined model NC catalysts revealed that both $Ag_{25}(SR)_{18}$ and $Au_{25}(SR)_{18}$ NCs facilitate a CO_2RR pathway through enhanced water dissociation (WD) kinetics. However, these NCs display significantly different HER behaviors under CO_2: $Au_{25}(SR)_{18}$ exhibits enhanced activity, while $Ag_{25}(SR)_{18}$ is significantly suppressed. Theoretical studies indicate that the enhanced WD kinetics stem from direct proton abstraction by the CO_2RR intermediate. Adsorption geometry analyses further demonstrate that their differing selectivities arise from distinct HER active sites, thereby explaining the variations in CO_2RR and HER activities between $Ag_{25}(SR)_{18}$ and $Au_{25}(SR)_{18}$ catalysts.

Received 8th September 2025,
Accepted 26th November 2025

DOI: 10.1039/d5ey00269a

rsc.li/eescatalysis

Broader context

The electrocatalytic CO_2 reduction reaction (CO_2RR) to CO offers a sustainable route to mitigate greenhouse gas emissions while producing a valuable feedstock for fuels and chemicals. Au and Ag are benchmark CO-selective catalysts, yet they display different behaviours under industrially relevant conditions: Au achieves low onset potentials but rapidly loses CO selectivity at high current densities, while Ag sustains CO production at high current densities. Here, we employ atomically precise nanoclusters, $Ag_{25}(SR)_{18}$ and $Au_{25}(SR)_{18}$ (SR = thiolate), to isolate the role of metal identity in the CO_2RR and the competing hydrogen evolution reaction (HER). Combining electrokinetic studies, *operando* infrared spectroscopy, and theoretical calculation, we reveal that both catalysts benefit from accelerated water dissociation in the presence of CO_2, but Au favours the HER due to weak *H binding, whereas Ag suppresses the HER through stronger *H binding, thereby maintaining CO selectivity. These molecular-level insights highlight that beyond *CO adsorption energy, interfacial proton dynamics and *H energetics govern CO_2RR selectivity, offering guidance for designing highly selective catalysts for scalable CO_2 utilization.

Introduction

The electrocatalytic CO_2 reduction reaction (CO_2RR) has emerged as a promising strategy to close the carbon cycle while simultaneously producing value-added fuels and chemicals.[1,2] Among various CO_2RR products, CO is of particular industrial relevance, as it serves as a key feedstock for syngas production[3] and polymer synthesis,[4] thereby sustaining strong market demand.[5] Au and Ag are known to selectively produce CO,[6] a feature attributed to their weak binding affinity for *CO intermediates.[7] Traditionally, Au-based electrodes have been regarded as more efficient than Ag-based electrodes for CO_2-to-CO conversion.[8–10] In 1994, Hori *et al.* demonstrated that Au electrodes exhibit superior CO_2RR performance compared to Ag electrodes, achieving lower overpotentials and higher CO selectivity at comparable current densities.[8] This observation is further supported by density functional theory (DFT)

---

[a] *Department of Chemistry, Yonsei University, Seoul, 03722, Republic of Korea. E-mail: dongil@yonsei.ac.kr*

[b] *School of Chemistry and Chemical Engineering, Chongqing Key Laboratory of Theoretical and Computational Chemistry, Chongqing University, Chongqing, 401331, China. E-mail: qingtang@cqu.edu.cn*

† H. S. and F. S. contributed equally to this work.

calculations, which indicate that the free energy barrier for the CO_2RR is lower on Au surfaces than on Ag surfaces.[10]

The advancement of gas diffusion electrode (GDE)-based flow electrolyzers has enabled the attainment of commercially feasible current densities for the CO_2RR by overcoming CO_2 mass transport constraints.[11] Although Au catalysts have traditionally been considered more effective than Ag catalysts for CO_2-to-CO electroreduction, recent research has indicated a notable inconsistency: Ag catalysts demonstrate a rise in CO production rates with increased overpotentials,[12–17] while Au catalysts[18–22] frequently reach a plateau or experience reduced selectivity with increasing applied potentials.

Fig. 1a shows CO partial current densities for various Ag and Au electrocatalysts as a function of applied potential (*vs.* standard hydrogen electrode, SHE). Au catalysts generally exhibit an earlier onset potential for CO production (approximately −0.9 V *vs.* SHE) compared to Ag catalysts (approximately −1.2 V *vs.* SHE).

This lower onset potential of Au is attributed to its optimal CO binding strength, as reported by Jaramillo *et al.* (Fig. 1b). Metals with weaker CO binding than Au (*e.g.*, Ag, Zn) exhibit reduced CO_2RR activity due to sluggish CO_2 activation, whereas those with stronger CO binding (Cu, Ni, and Pt) activate CO_2 effectively but are limited by slow CO desorption or further CO conversion.

Despite requiring higher overpotentials, Ag catalysts achieve steadily increasing CO current densities exceeding 400 mA cm^{-2}, while Au catalysts plateau at approximately 200 mA cm^{-2}. Ozden *et al.* reported that Au nanoparticles (NPs) exhibited declining CO selectivity above 100 mA cm^{-2}, whereas Ag NPs maintained high CO_2-to-CO conversion rates even at elevated overpotentials.[23] Similarly, Burdyny and co-workers found that Au-coated GDEs showed decreasing CO selectivity at high current densities, while Ag-coated GDEs retained strong CO selectivity.[24] These findings suggest that CO binding strength alone cannot account for the diverging behaviors observed under industrially relevant current densities.

Water dissociation (WD) is a crucial process in both the CO_2RR and hydrogen evolution reaction (HER), particularly under alkaline conditions.[25–27] Since both the CO_2RR and the HER entail proton transfer from H_2O to intermediates, the WD step significantly influences the provision of protons to the reaction interface. Nevertheless, the WD mechanism is frequently disregarded because of the challenges linked to theoretical modeling and experimental isolation. Additionally, traditional nanostructured catalysts encounter issues such as ambiguous active sites and non-uniform surfaces, which hinder the clarification of structure–activity relationships.

Atomically precise metal nanoclusters (NCs) have recently garnered significant attention due to their unique electrocatalytic properties.[28–31] Their atom-level precision represents a breakthrough in overcoming the limitations of traditional catalysts. These NCs can be synthesized with molecular purity, and their structures can be definitively determined by single-crystal X-ray diffraction (SC-XRD),[32] allowing for identification through specific molecular formulas such as $Au_{25}(SR)_{18}$, $Au_{144}(SR)_{60}$, $Ag_{25}(SR)_{18}$, and $Ni_6(SR)_{12}$, with SR denoting a thiolate ligand. Additionally, the presence of surface-protecting ligands provides exceptional stability to these NCs, even at ultrasmall sizes (<3 nm). Due to their precisely defined catalytic surfaces, metal NCs serve as valuable model catalysts for exploring fundamental catalytic mechanisms.

Kauffman *et al.* initially demonstrated that $Au_{25}(SR)_{18}$ NCs exhibit excellent CO_2RR activity attributed to their unique CO_2 adsorption sites containing tri-sulfur motifs.[33] Subsequent investigations utilizing $Au_{25}(SR)_{18}$, $Au_{38}(SR)_{24}$, and $Au_{144}(SR)_{60}$ NCs indicated that dethiolated Au sites bridging surface sulfur atoms and core Au atoms function as the active sites for electrochemical reduction of CO_2 to CO.[34] Recently, Au active sites have been effectively incorporated into other NC frameworks such as $Ag_{25}(SR)_{18}$[35] and $Ni_4(SR)_8$,[36] confirming the broad applicability and transferability of these active-site motifs. While $Ag_{25}(SR)_{18}$ NCs have demonstrated lower CO_2RR activity compared to Au_{25} NCs,[35] a direct evaluation of their CO_2RR performance and competition with the HER under industrially relevant conditions is yet to be documented.

Herein, we present a comparative analysis of CO_2RR and HER activities using $Ag_{25}(SPhMe_2)_{18}$, where $SPhMe_2$ = 2,4-dimethylbenzenethiolate, and $Au_{25}(SEtPh)_{18}$, where SEtPh = 2-phenylethanethiolate, as model catalysts. These two NCs,

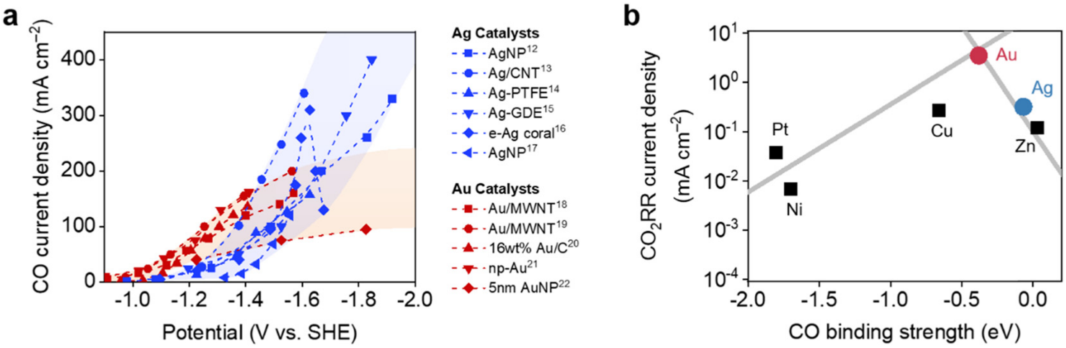

Fig. 1 (a) Benchmarks of CO current density values for AgNPs[12–17] and AuNPs[18–22] as a function of cathodic potential, with shaded regions serving as a visual guide. A pH-independent SHE scale is used to facilitate comparison across different experimental conditions. (b) CO current densities of different metal surfaces at −0.8 V *versus* RHE plotted against CO binding strength. Grey lines are incorporated as visual aids. Reproduced with permission from ref. 7. Copyright 2014 American Chemical Society.

hereafter abbreviated as Ag_{25} and Au_{25}, respectively, exhibit nearly identical geometric structures but differ only in their metal composition, allowing a direct comparison of their intrinsic catalytic performance at the atomic scale. Although Au_{25} is generally expected to exhibit superior performance compared to Ag_{25}, our results show that this is not always the case, particularly at high overpotentials (>0.3 V *vs.* reversible hydrogen electrode, RHE; all potentials are referenced to RHE unless stated otherwise), attributed to the presence of the competing HER. Electrokinetic and *in situ* spectroscopic analyses validate that WD kinetics are enhanced in the presence of CO_2 on both NCs. DFT calculations further demonstrate that disparities in hydrogen adsorption energies between Ag and Au significantly influence their divergent CO_2RR selectivities. These insights shed light on the enhanced CO selectivity of Ag_{25} at elevated current densities and offer valuable guidance for the development of next-generation electrocatalysts tailored for efficient industrial CO_2 conversion.

Results and discussion

CO_2RR activities of atomically precise Ag_{25} and Au_{25} NCs

To compare the catalytic properties of Ag and Au directly, we utilized atomically precise Ag_{25} and Au_{25} NCs as model catalysts. These NCs possess nearly identical atomic structures but vary only in their constituent metal atoms, allowing for an atomic-level exploration of the impact of metal identity in the CO_2RR. SC-XRD analysis clearly revealed their atomic structures.[32,37] Both Ag_{25} and Au_{25} NCs consist of an icosahedral Ag_{13} (or Au_{13}) core surrounded by six dimeric $Ag_2(SR)_3$ (or $Au_2(SR)_3$) staple motifs, as illustrated in Fig. 2a. The structural similarity between Ag_{25} and Au_{25} NCs offers an excellent basis for comparing catalytic properties using precisely defined catalyst structures.

We synthesized the Ag_{25} and Au_{25} NCs following procedures described elsewhere[32,37] with slight modifications (refer to the Methods section in the SI). The NCs were characterized using electrospray ionization (ESI) mass spectrometry and ultraviolet-visible (UV-vis) absorption spectroscopy. The ESI mass spectra displayed distinct single peaks (Fig. 2b and c), indicating the molecular purity of both NCs. Additionally, the experimentally observed peaks at 5167 and 7393 Da closely matched the isotope patterns for $Ag_{25}(SC_8H_9)_{18}^-$ and $Au_{25}(SC_8H_9)_{18}^-$ NC ions, respectively, confirming the atomically precise composition of the synthesized NCs (insets of Fig. 2b and c). The UV-vis absorption spectra of Ag_{25} and Au_{25} NCs also showed characteristic features consistent with previous findings (Fig. S1 in the SI).[37,38]

In our previous studies, we have shown that thiolate-protected metal NCs can be electrochemically activated by partially removing thiolate ligands.[34,35] Here, both Ag_{25} and Au_{25} NCs were activated through constant potential electrolysis (CPE) at −0.96 V for 2 h. The UV-vis absorption spectra of the activated Ag_{25} and Au_{25} NCs (Fig. S1 in the SI) remained nearly identical to those of the pristine NCs, indicating preservation of the NC structure during activation. X-ray photoelectron spectroscopy (XPS) analysis (Fig. S2a, b and Table S1 in the SI) confirmed a reduction in ligand content to approximately twelve thiolates, resulting in $Ag_{25}(SR)_{12}$ and $Au_{25}(SR)_{12}$ compositions. These compositions align with those previously reported for electrochemically activated Ag_{25} and Au_{25} NCs.[34,35] These findings suggest that electrochemical activation exposed an equivalent number of active sites on both NCs (Fig. S2c and d in the SI). Importantly, the activated NCs remained stable throughout subsequent CPE experiments (Fig. S3 in the SI). High-angle annular dark-field scanning transmission electron microscopy images of the recovered Ag_{25} and Au_{25} NCs after the CPE experiments (Fig. S4, SI) further verified that both NCs preserved their structural integrity, each exhibiting a diameter of approximately 1 nm.

The CO_2RR activities of the Ag_{25} and Au_{25} NCs were assessed through CPE experiments on NC/GDEs in a CO_2-fed flow electrolyzer using a 1.0 M KOH electrolyte solution (refer to the Methods section and Fig. S5 in the SI). All electrochemical measurements were conducted after the electrochemical activation process. Fig. 2d illustrates the CO partial current densities recorded for Au_{25} and Ag_{25} NCs. The Au_{25} NC demonstrated CO production commencing near zero overpotential, which initially increased but stabilized at 230 mA cm^{-2} below −0.5 V. In contrast, the Ag_{25} NC necessitated a slightly higher onset potential (−0.4 V) but exhibited a continuous rise in current density with increasing overpotential. The CO selectivity profiles of the NC catalysts also exhibited notable distinctions (Fig. 2e). The CO selectivity of Au_{25} NCs peaked at 98% at −0.2 V, declining significantly to 52% at −0.6 V. Conversely, the Ag_{25} NC demonstrated a CO selectivity of 76% near its onset potential, which progressively increased and remained above 92% even at −0.7 V. These findings align with previously reported trends for Ag and Au catalysts (Fig. 1a). Specifically, the CO current densities of Au catalysts tend to plateau or decrease at high overpotentials, while those of Ag catalysts continue to rise, highlighting a fundamental distinction in the catalytic behavior of Ag and Au surfaces.

Comparing CO_2RR and HER activities of NC catalysts

To gain a deeper understanding of the differing CO_2RR selectivities of Ag and Au electrocatalysts, we investigated their competing HER activities. Fig. 3a compares the CO and H_2 partial current densities of Ag_{25} and Au_{25} NCs under CO_2- and Ar-fed conditions, respectively. Notably, both NCs showed lower onset potentials for the CO_2RR compared to the HER, suggesting that the CO_2RR is more favorable than the HER on both catalysts.

Under neutral to alkaline conditions, the CO_2RR and HER proceed *via* the following elementary steps, where * denotes an active site:

CO_2RR:[39]

$$* + CO_2 + e^- \rightarrow *CO_2^- \tag{1}$$

$$*CO_2^- + H_2O \rightarrow *COOH + OH^- \tag{2}$$

$$*COOH + e^- \rightarrow *COOH^- \tag{3}$$

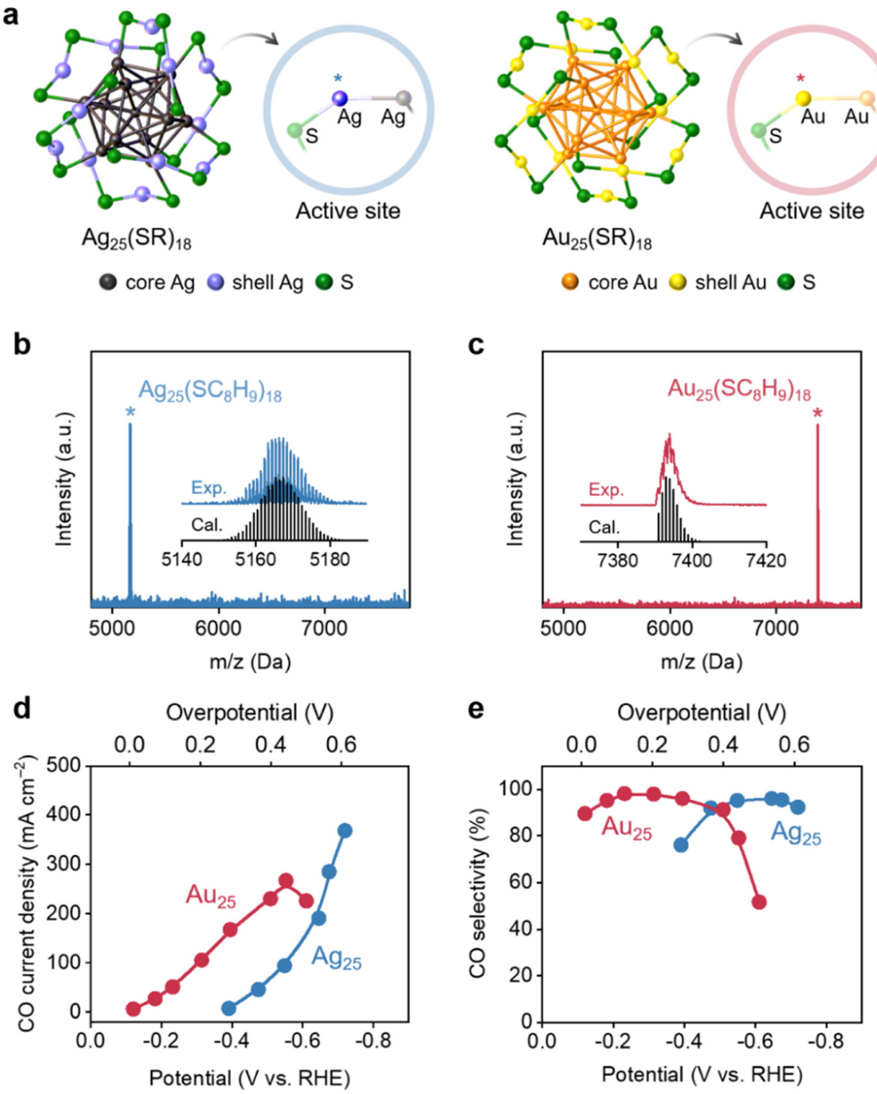

Fig. 2 (a) Crystal structures of $Ag_{25}(SR)_{18}^-$ and $Au_{25}(SR)_{18}^-$ NCs (adapted from ref. 36 and 31, respectively). Only the sulfur atoms of the thiolate ligands are depicted for clarity. The active site units of the NCs are highlighted in circles. Negative-mode ESI mass spectra of (b) Ag_{25} and (c) Au_{25} NCs. Insets compare the experimental (lines) and simulated (bars) isotope patterns of the NC ions. (d) CO current density and (e) CO selectivity measured for Ag_{25} and Au_{25} NCs at different cathodic potentials in a CO_2-fed flow electrolyzer using 1.0 M KOH as the electrolyte. All potentials were *iR*-corrected. In (d) and (e), the data represent averages from 2–3 independent experiments, and the error bars were smaller than the symbol size in the graphs.

$$*COOH^- \rightarrow *CO + OH^- \quad (4)$$

$$*CO \rightarrow * + CO \quad (5)$$

HER:[40]

$$* + H_2O + e^- \rightarrow *H + OH^- \quad (6)$$

$$*H + H_2O + e^- \rightarrow * + H_2 + OH^- \quad (7)$$

$$\text{or } 2*H \rightarrow 2* + H_2 \quad (8)$$

To further investigate the mechanistic origin of differences in CO_2RR and HER activities, electrokinetic studies were conducted. For the CO_2RR, the theoretical Tafel slopes are predicted to be 120 and 40 mV dec^{-1} when the first (eqn (1)) and second (eqn (3)) electron-transfer steps are rate-determining, respectively.[39,41] On conventional Ag and Au surfaces, the first electron-transfer step involving CO_2 adsorption is typically the potential-determining step (PDS).[19,42–44] However, the Ag_{25} and Au_{25} NCs exhibited notably lower Tafel slopes of 61 and 40 mV dec^{-1}, respectively (Fig. 3b), indicating enhanced facilitation of the first electron-transfer step on these clusters. Both NCs exhibited pH-independent and H/D isotope-independent CO_2RR activity (Fig. S6 in the SI), indicating that proton-transfer steps are not involved in the PDS. Therefore, the second electron-transfer step (eqn (3)) is likely the PDS for both catalysts. The higher Tafel slope of Ag_{25} compared to Au_{25} may be attributed to the slower electron transfer rate on the Ag_{25} NC (Fig. S7 in the SI). Conversely, for the HER under an Ar atmosphere, the Tafel slopes were measured to be 144 and 153 mV dec^{-1} for Ag_{25} and Au_{25} NCs, respectively (Fig. 3b),

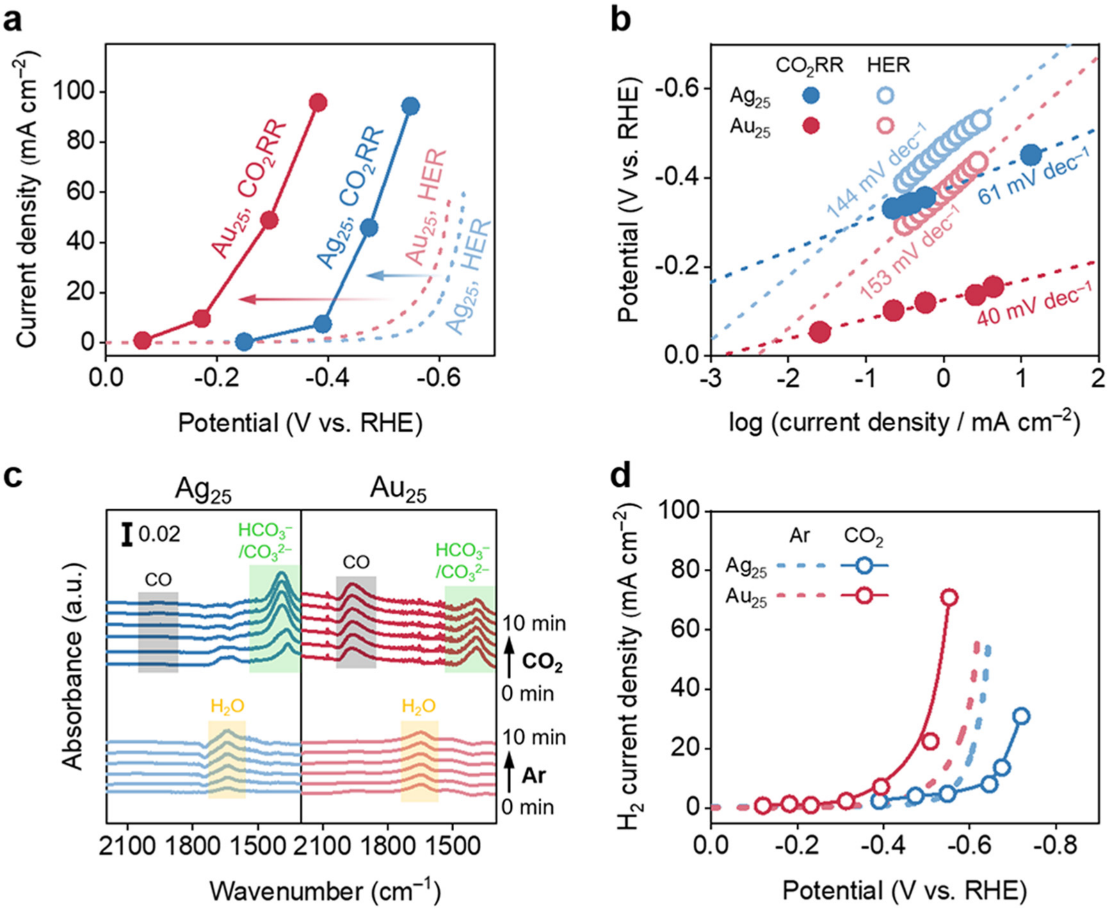

Fig. 3 (a) Comparison of the CO and H_2 current densities measured in the CO_2- and Ar-fed flow electrolyzer, respectively, on the Ag_{25}/GDE and Au_{25}/GDE. (b) Tafel plots for the CO_2-to-CO electroreduction and HER on the Ag_{25}/GDE and Au_{25}/GDE. (c) *In situ* ATR–FTIR spectra recorded on the Ag_{25}/GDE and Au_{25}/GDE in Ar- and CO_2-saturated 1.0 M $NaClO_4$ electrolyte solutions during the CPE measurement at −1.8 V *versus* SHE. (d) H_2 current densities measured on the Ag_{25}/GDE and Au_{25}/GDE in Ar- and CO_2-fed flow electrolyzers using a 1.0 M KOH electrolyte solution. The potentials in (a), (b), and (d) were *iR*-corrected.

indicating that the Volmer step involving water dissociation (eqn (6)) serves as the PDS on both catalysts.

As both the CO_2RR[25,26] and the HER[27] involve a WD step under alkaline conditions, the lower onset potential observed for the CO_2RR is surprising, considering the high energy barrier associated with this step.[45] One possible explanation is the generation of additional proton donors in the presence of CO_2. Both carbonic acid (H_2CO_3) and bicarbonate ions (HCO_3^-) can form under CO_2 conditions. However, the concentration of H_2CO_3 remains negligible due to the slow CO_2 hydration rate ($2.9 \times 10^{-2}\ s^{-1}$) and the rapid dissociation of H_2CO_3 ($3 \times 10^{6}\ s^{-1}$) under CO_2 conditions.[46] While HCO_3^- can serve as a viable proton donor for the CO_2RR[43,47] and the HER,[42,48] the experimentally determined reaction orders for the CO_2RR with respect to HCO_3^- were near-zero for both NCs (Fig. S8 in the SI), indicating that the contribution from HCO_3^- is negligible and that water is the dominant proton source in this system.

Another possibility is that the WD step itself is accelerated under CO_2 conditions. To directly assess WD kinetics, the NC/GDEs were subjected to *in situ* attenuated total reflection (ATR)–Fourier transform infrared (FTIR) absorption spectroscopy[49] during CPE experiments under Ar and CO_2 atmospheres (refer to the Methods section and Fig. S9 in the SI). A 1.0 M $NaClO_4$ electrolyte solution was utilized in this experiment to prevent interference from pre-existing bicarbonate ions.

Fig. 3c presents the *operando* FTIR spectra obtained from the Ag_{25}/GDE and Au_{25}/GDE during the CPE experiments. In the Ar environment, both NCs exhibited the H_2O bending mode (δHOH, ∼1645 cm^{-1}), indicating water molecules' accumulation near the negatively charged electrode surface due to hydrated cation layering.[50] Upon introducing CO_2 gas, noticeable spectral changes occurred. Two new vibrational bands emerged at approximately 1950 cm^{-1} and 1400 cm^{-1}, corresponding to the stretching mode of adsorbed *CO intermediates[51] (refer to Fig. S10a in the SI for Ag_{25}) and the asymmetric stretching of carbonate species (HCO_3^-/CO_3^{2-})[52] formed by CO_2 equilibrium. Simultaneously, the intensity of the δHOH band gradually decreased on Ag_{25} NCs, while it promptly vanished on Au_{25} NCs (Fig. 3c and Fig. S10b, c in the SI). This swift disappearance of the water bending peak under CO_2 conditions indicates a substantial reduction in accumulated water, implying enhanced WD kinetics in the presence of CO_2 for both NCs.

As discussed above, the Volmer step serves as the PDS for the HER on both Ag_{25} and Au_{25} NCs. Consequently, one would anticipate that improved WD kinetics would also enhance the HER performance of both NCs. However, while Au_{25} demonstrated increased HER activity under CO_2 compared to Ar (Fig. 3d), Ag_{25} exhibited a notable decline. This suggests that the augmented WD kinetics under CO_2 do not favor the HER kinetics of Ag_{25}. This divergent behavior highlights both the similarities and distinctions between Ag_{25} and Au_{25} NCs: although both show significantly lower onset potentials for the CO_2RR compared to the HER—attributable to the enhanced WD kinetics under CO_2—Au_{25} exhibits improved HER activity under CO_2, whereas Ag_{25} exhibits markedly suppressed HER activity under CO_2 flow.

DFT calculations

To comprehend the differing CO_2RR selectivities of Ag_{25} and Au_{25} NCs, we conducted DFT calculations using $Ag_{25}(SCH_3)_{17}^-$ and $Au_{25}(SCH_3)_{17}^-$ as model systems, representing their singly dethiolated forms (Fig. S11 in the SI). To ensure that protons were provided from water, the calculations were conducted with six explicit water solvent molecules. Initially, we computed the Gibbs free energies of crucial intermediates involved in the alkaline CO_2RR pathway on both NCs. As illustrated in Fig. 4a and Fig. S12 in the SI, the formation of the *COOH intermediate from $^*CO_2^-$ occurs with a low energy barrier (transition state 1, TS1), succeeded by *CO generation through a potential-determining electron transfer (transition state 2, TS2) for both NCs. Notably, the energy barrier for TS2 was lower on Au_{25} (1.07 eV) than on Ag_{25} (1.27 eV), aligning with the experimentally observed lower onset potential for the CO_2RR on Au_{25} (Fig. 2d).

Since the WD step plays a role in both the CO_2RR and HER, we compared the corresponding barriers between the Ag_{25} and Au_{25} NCs. Fig. S13 in the SI illustrates that the initial WD step acts as the PDS for the HER on both Ag_{25} and Au_{25} NCs, with energy barriers of 1.57 and 0.93 eV, respectively. A direct comparison of the WD barriers during the CO_2RR and the HER (Fig. 4b) indicates that WD proceeds more favorably during the CO_2RR than during the HER for both NCs. The adsorption configurations of crucial reaction intermediates offer valuable insights into the promotion of WD during the CO_2RR. As depicted in Fig. 4c, the formation of *COOH from $^*CO_2^-$ involves a direct proton transfer from a neighboring water molecule. This is attributed to the capability of $^*CO_2^-$ intermediates to nucleophilically abstract a proton from nearby water molecules, thereby reducing the activation barrier for proton transfer. Furthermore, the Au–COOH bond length (2.08 Å) was shorter than that of Ag–COOH (2.23 Å), indicating a stronger stabilization of the intermediate on Au_{25} and contributing to its enhanced CO_2RR kinetics.

Furthermore, the disparity in limiting potentials between the CO_2RR and the HER offers mechanistic insight into the selectivity profile (Fig. 4d). In the case of Ag_{25}, the limiting potential for the CO_2RR (1.27 eV) is significantly lower than that for the HER (1.57 eV), indicating a pronounced preference for the CO_2RR. Conversely, for Au_{25}, the limiting potentials for the CO_2RR (1.07 eV) and the HER (0.93 eV) are similar, explaining the experimentally observed decline in CO selectivity at elevated overpotentials (Fig. 2e). These computational results collectively demonstrate that the WD kinetics are significantly enhanced by direct proton abstraction by the $^*CO_2^-$ intermediates, resulting in a reduced kinetic barrier for *COOH formation and increased CO_2RR activity. A simplified schematic of this mechanistic pathway is depicted in Fig. 4e, emphasizing the contribution of $^*CO_2^-$ in expediting the WD step on both Ag and Au surfaces.

We will now compare the contrasting HER behaviors of Ag_{25} and Au_{25} NCs under CO_2 and Ar atmospheres, as shown in Fig. 3d. To clarify these distinctions, we examined the adsorption geometry of *H intermediates. Among the adsorption sites tested (Fig. S14 in the SI), the hollow sites at the Ag_3/Au_3 triangular facet exhibit the lowest hydrogen adsorption energies for both NCs. Accordingly, under an Ar atmosphere, the dissociated hydrogen from H_2O is adsorbed at the hollow site of the Ag_3 (Au_3) triangle, with distances of 1.88 Å and 2.44 Å from the central atom on Ag_{25} and Au_{25} NCs, respectively (Fig. 5). This observation suggests that the Au surface exhibits a weaker affinity for hydrogen in comparison to the Ag surface.

The difference in behavior can be attributed to stronger aurophilic (Au–Au) interactions[53,54] compared to argentophilic (Ag–Ag) interactions,[55] which arise from relativistic effects linked to the heavy atomic mass of Au. These effects lead to the contraction of the 6s orbital and the expansion of the 5d orbitals.[56,57] The expanded 5d orbitals not only enhance both Au–ligand and Au–Au bonding but also widen the d-state energy distribution, thereby reducing the binding strength with adsorbates.[58] Consistent with this, numerous Ag–H multinuclear complexes[59–61] and clusters[62,63] have been documented, while Au–H clusters[64,65] are comparatively rare. In our system, the weak Au_3–H binding likely results from this relativistic effect, which facilitates the easy release of the *H intermediate from the Au_3 triangle, ultimately promoting H_2 evolution.

The HER activity of Au_{25} is expected to increase further in the presence of CO_2. Calculations of alkaline HER reaction energetics with an adsorbed CO_2 molecule showed that, on Au_{25}, the dissociated H from H_2O relocates from the hollow site to the staple Au site, while on Ag_{25}, it remains at the strongly favored hollow site (Fig. S15 in the SI). Previous studies on the HER of Au_{25} catalysts have mainly focused on *H adsorption at the core atoms of the cluster.[66,67] However, it has also been reported that the preferred adsorption site can vary depending on the electronic structure of the catalyst.[68] Notably, the *H adsorption site can shift depending on the reaction environment. Compared with the alkaline HER in an Ar atmosphere, the calculated PDS barrier on Au_{25} decreases from 0.93 to 0.83 eV due to the participation of the more active staple Au site. Conversely, the PDS barrier on Ag_{25} increases from 1.57 to 1.65 eV in the presence of CO_2, possibly due to the competition with the CO_2RR. These results provide a clear explanation for the differing HER behaviors of Ag_{25} and Au_{25} NCs under CO_2 and Ar atmospheres.

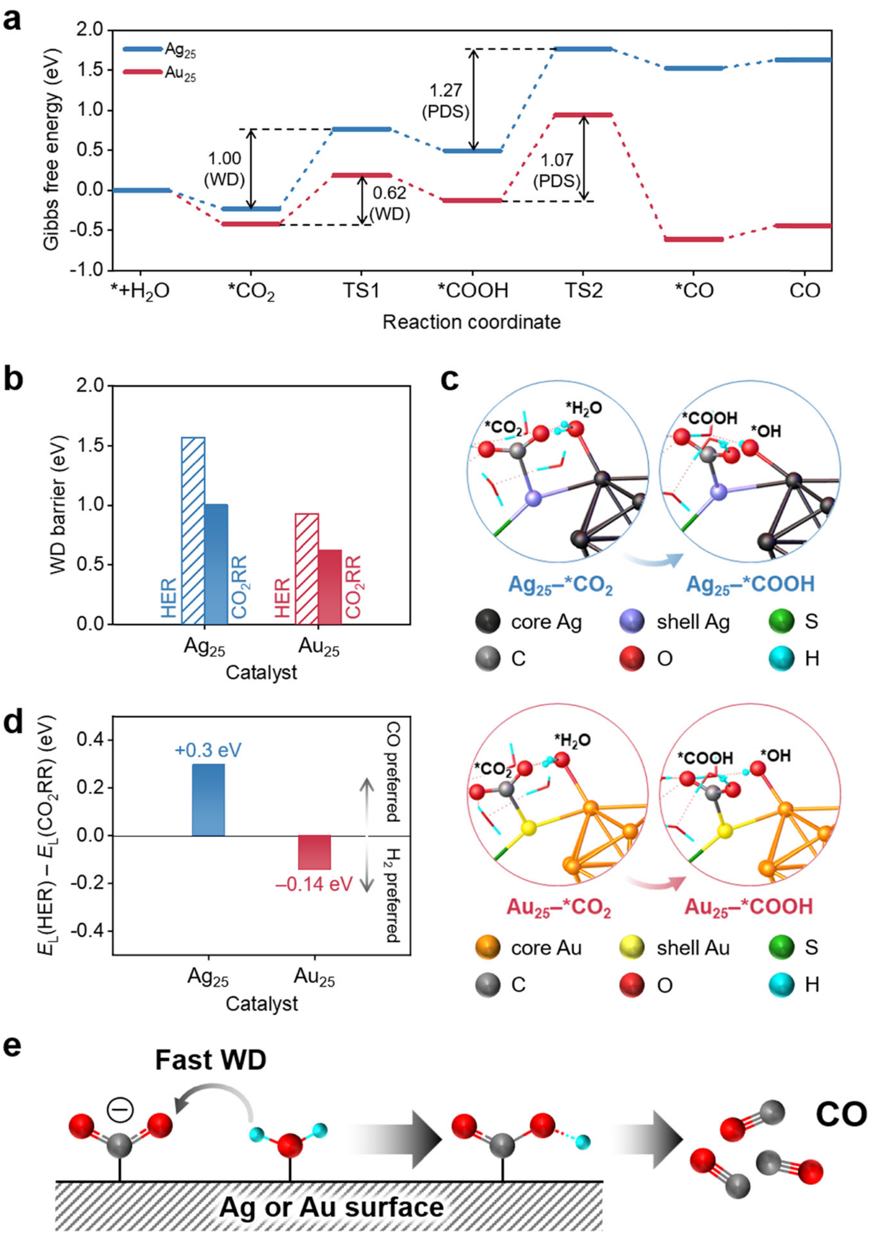

Fig. 4 (a) Free energy diagrams illustrating CO_2-to-CO reduction with six explicit water solvent molecules on $Ag_{25}(SCH_3)_{17}^-$ and $Au_{25}(SCH_3)_{17}^-$ NCs. (b) Comparison of WD energy barriers for the CO_2RR and HER on $Ag_{25}(SCH_3)_{17}^-$ and $Au_{25}(SCH_3)_{17}^-$ NCs. (c) Optimized intermediate structures of $^*CO_2^-$ and $^*COOH^-$ adsorbed onto $Ag_{25}(SCH_3)_{17}^-$ (blue circles) and $Au_{25}(SCH_3)_{17}^-$ (red circles). Only structures near the active sites are shown for clarity. (d) Differences in limiting potentials for the CO_2RR and HER on $Ag_{25}(SCH_3)_{17}^-$ and $Au_{25}(SCH_3)_{17}^-$ NCs. (e) Proposed mechanism of the alkaline CO_2RR occurring on Ag and Au surfaces.

To summarize, the DFT calculations unequivocally offer a molecular-level explanation for the distinct selectivities observed for the Ag_{25} and Au_{25} NCs. The WD step is significantly accelerated by the direct abstraction of protons by $^*CO_2^-$ intermediates during the CO_2RR on both NCs, thereby amplifying the CO_2RR. The disparate active sites implicated in the HER contribute to the differing HER performances of Ag_{25} and Au_{25} NCs. While the strongly adsorbed *H intermediate at the hollow site notably hinders the HER activity on Ag_{25}, the participation of the more active staple Au site significantly enhances the HER activity of Au_{25}, resulting in a preference for H_2 production over CO.

Finally, it is instructive to compare the catalytic behaviors of the model catalysts with those of more conventional catalysts. Fig. 6 illustrates CO_2RR and HER performances of commercial Ag and Au NP catalysts. Consistent with the patterns noted for Ag_{25} and Au_{25} NCs, Au NPs demonstrate a low onset potential for CO production but achieve a limiting current density of around 50 mA cm^{-2} (Fig. 6a). This is accompanied by a decrease in CO selectivity and an escalation in HER activity at high overpotentials. In contrast, Ag NPs exhibit a steadily increasing current, maintaining CO selectivity above 80% at elevated overpotentials (Fig. 6a). Notably, the divergent HER

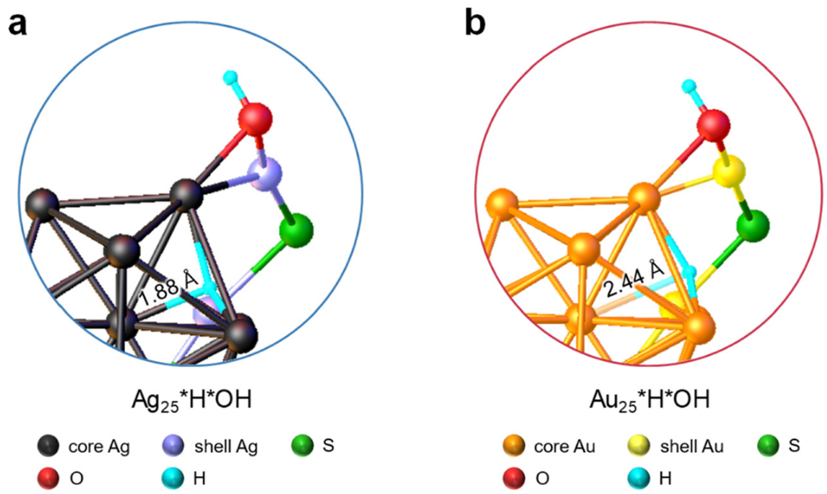

Fig. 5 Optimized intermediate structures of *H- and *OH co-adsorbed (a) $Ag_{25}(SCH_3)_{17}^-$ and (b) $Au_{25}(SCH_3)_{17}^-$. The alkyl chains and other five staple units are omitted for clarity.

behaviors of Ag_{25} and Au_{25} NCs are also evident for Ag and Au NPs (Fig. 6b). Specifically, relative to their HER activities under an Ar atmosphere, Au NPs exhibit enhanced HER activity, whereas Ag NPs exhibit diminished HER activity in the presence of CO_2, despite their markedly distinct structural characteristics, particularly the absence of ligand protection in the NPs in contrast to the NCs.

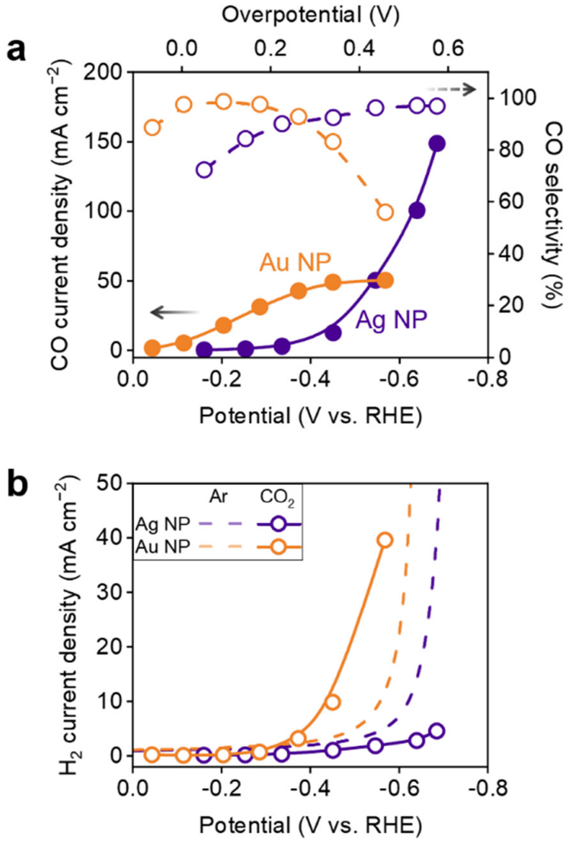

Fig. 6 (a) CO current densities and selectivities of Ag and Au NPs at different cathodic potentials in a CO_2-fed flow electrolyzer employing 1.0 M KOH as the electrolyte. (b) H_2 current densities of Ag and Au NPs in Ar- and CO_2-fed flow electrolyzers using 1.0 M KOH as the electrolyte. The potentials were *iR*-corrected.

Conclusions

In this study, we investigated the contrasting CO_2RR and HER behaviors of Ag and Au electrocatalysts. Leveraging the atomically well-defined surfaces of NC catalysts, we conducted a molecular-level analysis of their catalytic activities. We observed that while Au catalysts exhibit higher CO_2RR activity compared to Ag catalysts, they also exhibit significantly enhanced HER activity, leading to reduced CO selectivity. Electrokinetic and *operando* spectroscopic analyses indicated that both Ag_{25} and Au_{25} NCs demonstrate accelerated WD in the presence of CO_2, resulting in increased CO production over H_2. However, they exhibit distinct HER behaviors under CO_2 conditions: the HER activity of Au_{25} NCs is enhanced, whereas that of Ag_{25} NCs is notably suppressed. These findings are supported by DFT calculations, illustrating that WD kinetics are greatly influenced by direct proton abstraction by $*CO_2^-$ intermediates. Additionally, adsorption geometry analyses revealed their distinct active sites for the HER under CO_2, explaining the varying CO_2RR selectivities observed. Overall, this study highlights that well-defined, atomically precise NCs provide valuable molecular-level insights into CO_2RR and HER processes, which can be extrapolated to traditional catalysts.

Author contributions

H. S. and D. L. designed the project. H. S. carried out material synthesis and characterization, electrochemical test, and electrokinetic studies. F. S. performed the DFT calculation with Q. T.'s guidance. Q. T. and D. L. supervised the project. H. S. and D. L. wrote the manuscript. All authors discussed the results and provided comments on the manuscript at all stages.

Conflicts of interest

There are no conflicts to declare.

Data availability

The data supporting this article have been included as part of the supplementary information (SI). Supplementary information: methods, schematics of cell configurations, UV-vis and IR absorption spectra, XPS results, electrochemical data, and DFT calculation results. See DOI: https://doi.org/10.1039/d5ey00269a.

Acknowledgements

This work was supported by the National Research Foundation of Korea (NRF) grants (no. NRF-2022R1A2C3003610) and the Carbon-to-X Project (no. 2020M3H7A1096388) through the NRF funded by the Korean government (MSIT). The theoretical calculation was supported by the National Natural Science Foundation of China (no. 21903008) and the Chongqing Science and Technology Commission (cstc2020jcyjmsxmX0382).

Notes and references

1 Z. W. Seh, J. Kibsgaard, C. F. Dickens, I. Chorkendorff, J. K. Nørskov and T. F. Jaramillo, *Science*, 2017, **355**, eaad4998.

2 P. D. Luna, C. Hahn, D. Higgins, S. A. Jaffer, T. F. Jaramillo and E. H. Sargent, *Science*, 2019, **364**, eaav3506.

3 W. Choi, H. Seong, V. Efremov, Y. Lee, S. Im, D.-H. Lim, J. S. Yoo and D. Lee, *J. Chem. Phys.*, 2021, **155**, 014305.

4 S.-Y. Chen, R.-C. Pan, M. Chen, Y. Liu, C. Chen and X.-B. Lu, *J. Am. Chem. Soc.*, 2021, **143**, 10743–10750.

5 S. Nitopi, E. Bertheussen, S. B. Scott, X. Liu, A. K. Engstfeld, S. Horch, B. Seger, I. E. L. Stephens, K. Chan, C. Hahn, J. K. Nørskov, T. F. Jaramillo and I. Chorkendorff, *Chem. Rev.*, 2019, **119**, 7610–7672.

6 Y. Hori, in *Modern Aspects of Electrochemistry*, ed. C. G. Vayenas, R. E. White and M. E. Gamboa-Aldeco, Springer New York, New York, NY, 2008, pp. 89–189, DOI: 10.1007/978-0-387-49489-0_3.

7 K. P. Kuhl, T. Hatsukade, E. R. Cave, D. N. Abram, J. Kibsgaard and T. F. Jaramillo, *J. Am. Chem. Soc.*, 2014, **136**, 14107–14113.

8 Y. Hori, H. Wakebe, T. Tsukamoto and O. Koga, *Electrochim. Acta*, 1994, **39**, 1833–1839.

9 C. Delacourt, P. L. Ridgway and J. Newman, *J. Electrochem. Soc.*, 2010, **157**, B1902.

10 S. Back, M. S. Yeom and Y. Jung, *ACS Catal.*, 2015, **5**, 5089–5096.

11 D. M. Weekes, D. A. Salvatore, A. Reyes, A. Huang and C. P. Berlinguette, *Acc. Chem. Res.*, 2018, **51**, 910–918.

12 S. Verma, X. Lu, S. Ma, R. I. Masel and P. J. A. Kenis, *Phys. Chem. Chem. Phys.*, 2016, **18**, 7075–7084.

13 S. Ma, R. Luo, J. I. Gold, A. Z. Yu, B. Kim and P. J. A. Kenis, *J. Mater. Chem. A*, 2016, **4**, 8573–8578.

14 C.-T. Dinh, F. P. García de Arquer, D. Sinton and E. H. Sargent, *ACS Energy Lett.*, 2018, **3**, 2835–2840.

15 R. Wang, H. Haspel, A. Pustovarenko, A. Dikhtiarenko, A. Russkikh, G. Shterk, D. Osadchii, S. Ould-Chikh, M. Ma, W. A. Smith, K. Takanabe, F. Kapteijn and J. Gascon, *ACS Energy Lett.*, 2019, **4**, 2024–2031.

16 W. H. Lee, Y.-J. Ko, Y. Choi, S. Y. Lee, C. H. Choi, Y. J. Hwang, B. K. Min, P. Strasser and H.-S. Oh, *Nano Energy*, 2020, **76**, 105030.

17 C. Chen, Y. Li, S. Yu, S. Louisia, J. Jin, M. Li, M. B. Ross and P. Yang, *Joule*, 2020, **4**, 1688–1699.

18 H.-R. M. Jhong, C. E. Tornow, C. Kim, S. Verma, J. L. Oberst, P. S. Anderson, A. A. Gewirth, T. Fujigaya, N. Nakashima and P. J. A. Kenis, *Chem. Phys. Chem.*, 2017, **18**, 3274–3279.

19 S. Verma, Y. Hamasaki, C. Kim, W. Huang, S. Lu, H.-R. M. Jhong, A. A. Gewirth, T. Fujigaya, N. Nakashima and P. J. A. Kenis, *ACS Energy Lett.*, 2018, **3**, 193–198.

20 R. Shi, J. Guo, X. Zhang, G. I. N. Waterhouse, Z. Han, Y. Zhao, L. Shang, C. Zhou, L. Jiang and T. Zhang, *Nat. Commun.*, 2020, **11**, 3028.

21 A. Q. Fenwick, A. J. Welch, X. Li, I. Sullivan, J. S. DuChene, C. Xiang and H. A. Atwater, *ACS Energy Lett.*, 2022, **7**, 871–879.

22 S. Alinejad, J. Quinson, G. K. H. Wiberg, N. Schlegel, D. Zhang, Y. Li, S. Reichenberger, S. Barcikowski and M. Arenz, *ChemElectroChem*, 2022, **9**, e202200341.

23 A. Ozden, Y. Liu, C.-T. Dinh, J. Li, P. Ou, F. P. García de Arquer, E. H. Sargent and D. Sinton, *ACS Appl. Energy Mater.*, 2021, **4**, 7504–7512.

24 M. Sassenburg, R. de Rooij, N. T. Nesbitt, R. Kas, S. Chandrashekar, N. J. Firet, K. Yang, K. Liu, M. A. Blommaert, M. Kolen, D. Ripepi, W. A. Smith and T. Burdyny, *ACS Appl. Energy Mater.*, 2022, **5**, 5983–5994.

25 J. A. Gauthier, Z. Lin, M. Head-Gordon and A. T. Bell, *ACS Energy Lett.*, 2022, **7**, 1679–1686.

26 H. Ooka, M. C. Figueiredo and M. T. M. Koper, *Langmuir*, 2017, **33**, 9307–9313.

27 R. Subbaraman, D. Tripkovic, D. Strmcnik, K.-C. Chang, M. Uchimura, A. P. Paulikas, V. Stamenkovic and N. M. Markovic, *Science*, 2011, **334**, 1256–1260.

28 K. Kwak and D. Lee, *Acc. Chem. Res.*, 2019, **52**, 12–22.

29 S. Zhao, R. Jin and R. Jin, *ACS Energy Lett.*, 2018, **3**, 452–462.

30 Y. Du, H. Sheng, D. Astruc and M. Zhu, *Chem. Rev.*, 2020, **120**, 526–622.

31 B. Kumar, T. Kawawaki, N. Shimizu, Y. Imai, D. Suzuki, S. Hossain, L. V. Nair and Y. Negishi, *Nanoscale*, 2020, **12**, 9969–9979.

32 M. W. Heaven, A. Dass, P. S. White, K. M. Holt and R. W. Murray, *J. Am. Chem. Soc.*, 2008, **130**, 3754–3755.

33 D. R. Kauffman, D. Alfonso, C. Matranga, H. Qian and R. Jin, *J. Am. Chem. Soc.*, 2012, **134**, 10237–10243.

34 H. Seong, V. Efremov, G. Park, H. Kim, J. S. Yoo and D. Lee, *Angew. Chem., Int. Ed.*, 2021, **60**, 14563–14570.

35 H. Seong, M. Choi, S. Park, H.-W. Kim, J. Kim, W. Kim, J. S. Yoo and D. Lee, *ACS Energy Lett.*, 2022, **7**, 4177–4184.

36 H. Seong, Y. Jo, V. Efremov, Y. Kim, S. Park, S. M. Han, K. Chang, J. Park, W. Choi, W. Kim, C. H. Choi, J. S. Yoo and D. Lee, *J. Am. Chem. Soc.*, 2023, **145**, 2152–2160.
37 C. P. Joshi, M. S. Bootharaju, M. J. Alhilaly and O. M. Bakr, *J. Am. Chem. Soc.*, 2015, **137**, 11578–11581.
38 M. Zhu, C. M. Aikens, F. J. Hollander, G. C. Schatz and R. Jin, *J. Am. Chem. Soc.*, 2008, **130**, 5883–5885.
39 W. Deng, P. Zhang, B. Seger and J. Gong, *Nat. Commun.*, 2022, **13**, 803.
40 N. Mahmood, Y. Yao, J.-W. Zhang, L. Pan, X. Zhang and J.-J. Zou, *Adv. Sci.*, 2018, **5**, 1700464.
41 S. Fletcher, *J. Solid State Electrochem.*, 2009, **13**, 537–549.
42 A. Wuttig, M. Yaguchi, K. Motobayashi, M. Osawa and Y. Surendranath, *Proc. Natl. Acad. Sci. U. S. A.*, 2016, **113**, E4585–E4593.
43 Y. Chen, C. W. Li and M. W. Kanan, *J. Am. Chem. Soc.*, 2012, **134**, 19969–19972.
44 M. Ma, B. J. Trześniewski, J. Xie and W. A. Smith, *Angew. Chem., Int. Ed.*, 2016, **55**, 9748–9752.
45 S. Z. Oener, M. J. Foster and S. W. Boettcher, *Science*, 2020, **369**, 1099–1103.
46 K. Adamczyk, M. Prémont-Schwarz, D. Pines, E. Pines and E. T. J. Nibbering, *Science*, 2009, **326**, 1690–1694.
47 G. Marcandalli, A. Goyal and M. T. M. Koper, *ACS Catal.*, 2021, **11**, 4936–4945.
48 M. N. Jackson, O. Jung, H. C. Lamotte and Y. Surendranath, *ACS Catal.*, 2019, **9**, 3737–3743.
49 S. Zhu, T. Li, W.-B. Cai and M. Shao, *ACS Energy Lett.*, 2019, **4**, 682–689.
50 S. Banerjee, Z.-Q. Zhang, A. S. Hall and V. S. Thoi, *ACS Catal.*, 2020, **10**, 9907–9914.
51 S. Zhu, Q. Wang, X. Qin, M. Gu, R. Tao, B. P. Lee, L. Zhang, Y. Yao, T. Li and M. Shao, *Adv. Energy Mater.*, 2018, **8**, 1802238.
52 M. Moradzaman and G. Mul, *ACS Catal.*, 2020, **10**, 8049–8057.
53 A. Bayler, A. Schier, G. A. Bowmaker and H. Schmidbaur, *J. Am. Chem. Soc.*, 1996, **118**, 7006–7007.
54 A. Codina, E. J. Fernández, P. G. Jones, A. Laguna, J. M. López-de-Luzuriaga, M. Monge, M. E. Olmos, J. Pérez and M. A. Rodríguez, *J. Am. Chem. Soc.*, 2002, **124**, 6781–6786.
55 H. Schmidbaur and A. Schier, *Angew. Chem., Int. Ed.*, 2015, **54**, 746–784.
56 P. Pyykko and J. P. Desclaux, *Acc. Chem. Res.*, 1979, **12**, 276–281.
57 D. J. Gorin and F. D. Toste, *Nature*, 2007, **446**, 395–403.
58 N. Runeberg, M. Schütz and H.-J. Werner, *J. Chem. Phys.*, 1999, **110**, 7210–7215.
59 H. Z. Ma, J. M. White, R. J. Mulder, G. E. Reid, A. J. Canty and R. A. J. O'Hair, *Dalton Trans.*, 2018, **47**, 14713–14725.
60 A. Zavras, G. N. Khairallah, T. U. Connell, J. M. White, A. J. Edwards, P. S. Donnelly and R. A. J. O'Hair, *Angew. Chem., Int. Ed.*, 2013, **52**, 8391–8394.
61 A. W. Cook, T.-A. D. Nguyen, W. R. Buratto, G. Wu and T. W. Hayton, *Inorg. Chem.*, 2016, **55**, 12435–12440.
62 M. S. Bootharaju, R. Dey, L. E. Gevers, M. N. Hedhili, J.-M. Basset and O. M. Bakr, *J. Am. Chem. Soc.*, 2016, **138**, 13770–13773.
63 X. Yuan, C. Sun, X. Li, S. Malola, B. K. Teo, H. Häkkinen, L.-S. Zheng and N. Zheng, *J. Am. Chem. Soc.*, 2019, **141**, 11905–11911.
64 S. Takano, H. Hirai, S. Muramatsu and T. Tsukuda, *J. Am. Chem. Soc.*, 2018, **140**, 8380–8383.
65 V. K. Kulkarni, B. N. Khiarak, S. Takano, S. Malola, E. L. Albright, T. I. Levchenko, M. D. Aloisio, C.-T. Dinh, T. Tsukuda, H. Häkkinen and C. M. Crudden, *J. Am. Chem. Soc.*, 2022, **144**, 9000–9006.
66 K. Kwak, W. Choi, Q. Tang, M. Kim, Y. Lee, D.-E. Jiang and D. Lee, *Nat. Commun.*, 2017, **8**, 14723.
67 G. Hu, Q. Tang, D. Lee, Z. Wu and D.-E. Jiang, *Chem. Mater.*, 2017, **29**, 4840–4847.
68 O. López-Estrada, N. Mammen, L. Laverdure, M. M. Melander, H. Häkkinen and K. Honkala, *ACS Catal.*, 2023, **13**, 8997–9006.